

A Lunar-based Soft X-ray Imager (LSXI) for the Earth's magnetosphere

Guo Yihong¹, Wang Chi^{1,2*}, Wei Fei¹, Sun Tianran¹, Yu Xizheng¹, Peng Songwu¹, Graziella Branduardi-Raymont³, Steven Sembay⁴

1 National Space Science Center, Chinese Academy of Sciences, Beijing, 100190 China

2 University of Chinese Academy of Sciences, Beijing, 100049 China

3. University College London, Department of Space and Climate Physics, Mullard Space Science Laboratory, Holmbury St. Mary Dorking Surrey, RH5 6NT, United Kingdom

4 The University of Leicester, University Road, Leicester, LE1 7RH, United Kingdom

** Corresponding Author: cw@nssc.ac.cn*

Abstract: We propose to use the Moon as a platform to obtain a global view of Earth's magnetosphere by a Lunar-based Soft X-ray Imager (LSXI). LSXI is a wide field-of-view Soft X-ray telescope, which can obtain X-ray image of Earth's magnetosphere based on the solar wind charge exchange (SWCX) X-ray emission. Global perspective is crucial to understand the overall interaction of the solar wind with magnetosphere. LSXI is capable of continuously monitoring the evolution of geospace conditions under the impact of the solar wind by simultaneous observation of the bow shock, magnetosheath, magnetopause and cusps for the first time. This proposal is answering the call for the Chinese Lunar Exploration Program Phase IV.

Key words: Soft X-ray imager, lunar, magnetosphere, micro-pore optics

1. Introduction

Solar activities are important driving factors that affect the Earth's space environment, namely space weather. The space weather could seriously interfere with the normal operation of communication, navigation and space-based technology systems, and create broad and profound impact on social activities and economy. The solar wind squeezes or stretches the outer boundary of the Earth's magnetosphere and couples with the near-Earth space environment, causing geomagnetic disturbances and dramatic changes in charged particles which endangers the space activities. Observing the Earth's magnetosphere in a global view could significantly improve the ability of space weather forecast [Collier et al., 2010].

For the past fifty years, based on a number of magnetospheric satellites, we have built a revolutionary understanding of magnetosphere structure and the physical evolutionary process. At present, the majority of our knowledge of magnetospheric response to solar activities comes from in situ measurements by satellites in different locations, and theoretical model analysis. Missions, such as *Cluster* and *Double Star*, have provided important information about the local plasma [Credland et al., 1997; Liu

et al., 2005]. However, due to the limited observation points, it is difficult to fully reveal the overall interactions of the solar wind with the magnetosphere at the system level and to predict the global dynamics.

Recently, a novel soft X-ray imaging technique has been developed, which is inspired by the lobster eye structure [Branduardi-Raymont et al., 2012; Collier et al., 2012; Walsh et al., 2016]. This new type of instrument is a wide-field of view soft X-ray telescope with spectroscopic capabilities, and the detection principle is based on the recent discovery of solar wind charge exchange (SWCX) X-ray emission. The Soft X-ray Imager payloads on missions, such as SMILE (field of view is $16^{\circ}\times 27^{\circ}$), and the much smaller NanoSat CuPID (field of view is $5^{\circ}\times 5^{\circ}$), have adopted this technique and will become powerful diagnostic tools to study the geospace environment under various solar wind conditions in the future [Wang and Branduardi-Raymont, 2018, Camps, 2019]. These missions will be the breakthrough in this area. Nevertheless, they have spatial and temporal limitations to monitor the global magnetosphere. For this reason, the next generation of X-ray imaging instruments, located outside of the Earth's magnetosphere with a large field of view and long-term observation capability, are urgently required. The Moon can be used as an ideal location to set the instrument for observation purpose.

China started the lunar exploration project - "Chinese Lunar Exploration Program" (CLEP) in 2004, which initially includes three Phases: Orbiting, Landing, and Returning. On 24th November 2020, Chang'e-5 was launched to implement lunar sampling and return on 17th December, which marks the completion of CLEP's first three Phases. Previously, on 3rd January 2019, Chang'e-4 lunar probe successfully landed on the far-side of the Moon and returned the world's first lunar far side close-up image [Wu et al., 2020]. It was the first mission of Phase IV of CLEP, which starts a new chapter in the human lunar exploration. In addition, several missions will follow up, and complete the Phase IV of CLEP. Eventually, China will explore the polar region of the Moon and build a robotic lunar scientific research station, which can support long-term, large-scale scientific exploration for space science and space applications [Li et al., 2019; Zhao and Wang, 2019; Xu et al., 2019].

In the context of CLEP Phase IV, one of the application objectives is Moon-based observation and research of the Earth. Here we propose a Lunar-based Soft X-ray imager (LSXI). Compared to satellite payloads in close or extended terrestrial orbits, LSXI will achieve an unprecedented observational coverage of the magnetosphere and monitor the full chain interaction process of the solar wind and magnetosphere. Besides,

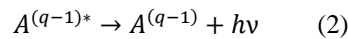
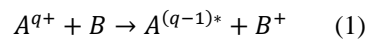
there are several additional favorable conditions for settling an X-ray imager on the Moon. As a stable facility, LSXI is maintainable, so that it has much longer operation life time to cover more than one solar activity period. The temperature in the lunar polar region is low which is beneficial to the instrument thermal stability, and so on. The project is proposed by National Space Science Center, Chinese Academy of Sciences, in collaboration with the Mullard Space Science Laboratory, University of Leicester (UK), and other research institutions and universities.

2. Science Objectives

2.1 Solar Wind Charge exchange process

The interaction between the solar wind and the terrestrial magnetic field forms the Earth's magnetopause. The solar wind charge exchange (SWCX) process is the basic mechanism of soft X-ray emission in the magnetosheath and cusp regions (Figure 1). It has been recognized as a significant source of solar system X-ray emission in recent years [Bhardwaj et al., 2007]. SWCX was first proposed to explain X-ray emission from the comet Hyakutake observed by the Rontgen Satellite (ROSAT) [Cravens, 1997; Lisse et al., 1996]. Such emission has also been detected in the vicinity of the Earth's magnetosphere by XMM-Newton and Suzaku [Snowden et al., 2004; Fujimoto et al., 2007].

In the geospace environment, high-temperature heavy ions in the solar wind collide with the neutral atoms or molecules coming out from the outer layers of the Earth's atmosphere. The heavy ion gains an electron in an excited state (Eq.1), and then decays to the lower energy state with soft X-ray radiation (Eq.2).



A is the heavy ion in the solar wind, i.e. oxygen, and B is the neutral atom such as the hydrogen in the Earth's exosphere. The SWCX spectrum is characterized by emission lines corresponding to the ion species present in the solar wind. The solar wind contains heavy elements such as C, O, Mg, Fe and Ne [Schwadron and Cravens, 2000]. The relative abundances of the elements are dependent on the conditions of the Sun. SWCX mainly concentrates in the energy range of 0.2~2.5keV.

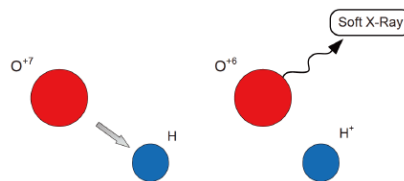


Figure 1 Solar wind Charge exchange mechanism

The SWCX X-ray flux I for a particular line of sight can be estimated by the line integration of volume emission rate P [Cravens, 2000]:

$$I = \frac{1}{4\pi} \int P dr = \frac{1}{4\pi} \int \alpha n_H n_{sw} \langle g \rangle dr \text{ (keVcm}^{-2}\text{s}^{-1}\text{sr}^{-1}) \quad (3)$$

Where α is the efficiency factor [Cravens, 1997], n_H and n_{sw} are number densities of the exospheric hydrogen and solar wind protons. The velocity $\langle g \rangle$ is the collision speed estimated by the solar wind speed u_{sw} and thermal speed u_{th} : $\langle g \rangle = \sqrt{u_{sw}^2 + u_{th}^2}$ [Sun et al., 2015].

The solar wind plasma is compressed after the bow shock, and basically cannot directly penetrate the magnetopause. It leads to a sharp boundary at the magnetopause where the intense soft X-ray photons are emitted. The solar wind can directly enter the Earth's pole region and thus the X-ray emission is intense in this area [Robertson and Cravens, 2003]. We can also find out the information about the composition of the solar wind from the SWCX emission. The discovery of SWCX X-ray emission provides a novel way for imaging the magnetosphere, and offers a new path to study solar wind-magnetosphere coupling [Branduardi-Raymont et al., 2012]. These observations would help to evaluate the effect of the space environment and validate global models of solar-terrestrial interactions.

2.2 Scientific goals and Questions

The solar wind-magnetosphere coupling and its dynamic process are the basic driving factors for space weather. To understand its physical connotation, it is necessary to understand the processes of global scale responses, mass and energy transportation, and the coupling between different regions. However, relying on single-point or multi-point in-situ measurements is not enough for grasping the global effects caused by the solar wind disturbance, which is the key to understand how the Sun affects and controls the plasma and space weather. Scientific issues expected to be addressed by global scale X-ray imaging include, but are not limited to, those summarized as follow (Table 1).

Table 1 Scientific goals and questions

Scientific Goals	Questions
<ul style="list-style-type: none"> Understanding the solar wind-magnetosphere interaction on the whole dayside magnetopause 	1) What are the global scale features of the reconnection region on the magnetopause?
	2) How does the magnetopause reconnection develop in different regions (latitudes and longitudes) on the whole dayside magnetopause?
	3) When and where does the steady and unsteady magnetopause reconnection

	dominate on the dayside magnetopause?
<ul style="list-style-type: none"> ● Showing the entire path of energy, mass or momentum transfer from solar wind into the magnetosphere through the cusps. 	1) How does the energy, mass or momentum transfer from the high altitude cusp to the low altitude cusp?
	2) How does the magnetic reconnection process develop after its interaction with cusps?
	3) How does the cusp/magnetopause asymmetry occur (caused by dipole tilt, time-dependent reconnection, and etc)?
<ul style="list-style-type: none"> ● Investigating the response of the geospace to solar wind disturbances. 	1) How does the solar wind-magnetopause interaction mode depend on the solar wind variations?
	2) How does the process of energy, mass or momentum transfer depend on solar wind conditions?
	3) What are the global scale responses of the geospace environment to extreme solar wind perturbations?

3. Payload Design Concept

3.1 Imaging method

The Soft X-ray wavelength ranges from 0.1nm to 10nm (0.124~1.24keV). X-ray focusing can only be obtained in a grazing incident optical system. The conventional X-ray imaging method (such as Wolter type I of telescope) has a practical observation field of view (FOV) around 1°. In order to achieve a wide field of view with low mass, we adopt the optical design based on the lobster-eye structure proposed by Angel [Angel, 1979]. Lobster-eye optics plate consists of millions of cube-shaped micro channels, and the ultra-smooth inner wall of the microchannel forms an X-ray reflective surface (Figure 2). The incident X-rays are sequentially reflected by two side perpendicular walls, and finally focused to a point to realize the imaging function. This imaging system makes the observation field of view theoretically extended to 4π .

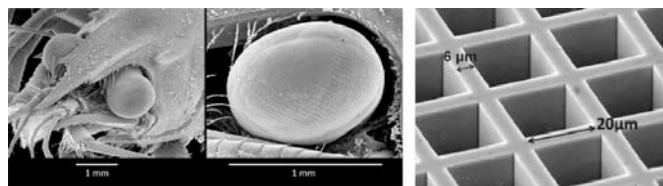


Figure 2 Images on the left and center show close-up views of a crustacean's eyes; the image on the right shows a manmade microchannel plate (www.nasa.gov)

The imaging element is a spherical microchannel plate (MCP). When parallel or point X-rays beam encounter the model, there will be a cross shape result on the focal plane (Figure 3). X-ray beams come from point A can be divided into three groups. The first group of rays (marked OO) reflect an odd number of times from adjacent walls and focus at the center of the cross; such rays form a true image. The second group of rays (marked OE and EO) have an odd-even pattern of reflections, the most common being a single reflection off one wall, and form the characteristic cross arm pattern. Other rays which either pass straight through (i.e. rays marked EE) or reflect an even number times in both adjacent walls form effectively a collimated background. The color of the point represents the number of reflections that the ray suffers in micro-channel, as shown in scatter diagram on image plane (Figure 3b). The rays, with different number of reflections, are reflected to different regions. The rays with twice reflections (marked in green) focus to the true focal spot. Two arms are formed by rays with once (marked in blue) or 3-time (marked in red) reflections in the micro-channel. The rays without reflection (marked in black) form the background. The lobster eye optic system can image both finite targets and targets at effective infinity. Due to the symmetric structure, there is no fixed optical axis, and the imaging ability is the same in any direction. Comparing with the conventional grazing incidence reflection optical system such as Wolter type telescope, the lobster eye imaging system has large FOV and high light collecting efficiency at the expense of angular resolution for similar resources.

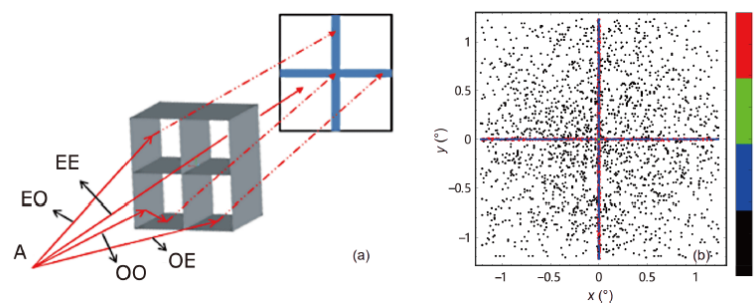


Figure 3 (a) Lobster eye imaging principle, (b) Scatter diagram distribution on image surface

3.2 Payload requirement and Design

LSXI will provide a large field of view and high energy resolution to map the SWCX X-ray emission. The primary scientific energy range is from 200eV to 2.5keV. As a goal, the energy band may extend up to 5keV to characterize the cosmic X-ray background. The preliminary design of LSXI has a FOV about $15^{\circ} \times 30^{\circ}$, corresponding to the region of $14.5 \times 29R_E$ near the Earth, which could cover the bow shock, magnetopause and cusps. The spatial resolution is around 6 arcmin (FWHM), which corresponds to $\sim 0.1R_E$ of the magnetopause. It meets the $0.5R_E$ scientific requirement. The capture cadences are on the order of minute(s) to track the dynamic motion of the magnetosphere. LSXI optics will be installed with an array of MCP in accordance with a spherical surface structure (Figure 4a). The MCP array components are implemented by a bundle of stretched quartz glass fiber. The bundle is organized into squares, and made into slices

with curvature of R , and the instrumental focal length is $R/2$. The MCP has ultra-smooth inner walls coated with metal for increasing the X-ray reflectivity (Figure 4b). The similar MCP plates have been used on the payloads of SMILE, Einstein Probe and SVOM and Einstein Probe [Gotz et al., 2015; Yuan et al., 2018].

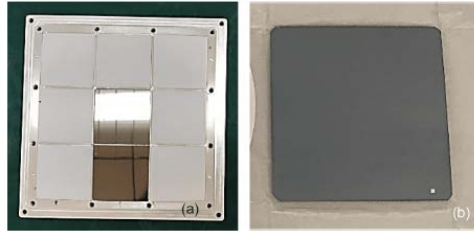


Figure 4 (a) schematic diagram of MCP holding structure, (b) MCP coated with Ir

The curvature of the MCP is proportional to the effective area which affects the imaging sensitivity. There is a trade-off between maximizing effective area and maximizing the FOV [Peng et al., 2019], subject to the science objectives and the available payload resources. For LSXI, the imaging sensitivity and the instrument compactness should be considered in the optical design. Theoretical effective area changes with radius of curvature in 0.5keV (Figure 5a). Three curves represent the different MPO parameter condition. The width of pores is $40\mu\text{m}$, and the plate thicknesses are 1.2mm, 1.6mm, and 2mm respectively. Larger radius of curvature leads to larger effective area, and the proper design of instrument parameters requires further calculation and analysis in the follow-up study.

The LSXI focal plane will employ large area X-ray sensitive CCDs. The size of the focal plane is approximately one quarter of the physical optic area. MCP and CCD sensors jointly determine the spatial and time resolution. The focal plane is formed with several detectors spliced side by side. The image data frame transfer rate of the CCD sensor and the working ability of the signal readout processing system should achieve a time resolution better than 10 second. The anticipated energy resolution should achieve 50eV at 0.5keV. The total effective area curve (lines in black) for the whole instrument response varies with incident energy of X-ray (Figure 5b), which represents the response function of the instrument. The red curve represents how the optic effective area varies with X-ray energy. The MCP radius of curvature is 60cm; plate thickness is 1.2mm and micro pore width is $40\mu\text{m}$. The influence of the absorption of optical blocking filter (Al 80nm +Polyamide 200nm) and the detector quantum efficiency (QE) are considered. It is anticipated the use of similar filter response (Figure 5c) and detector QE (Figure 5d) employed by the SMILE Soft X-ray imager. From the analysis of the observed target variation characteristics, the time scale of the morphological change of

the science objective is in the order of minutes to hours. LSXI main performance parameters as below (Table 2)

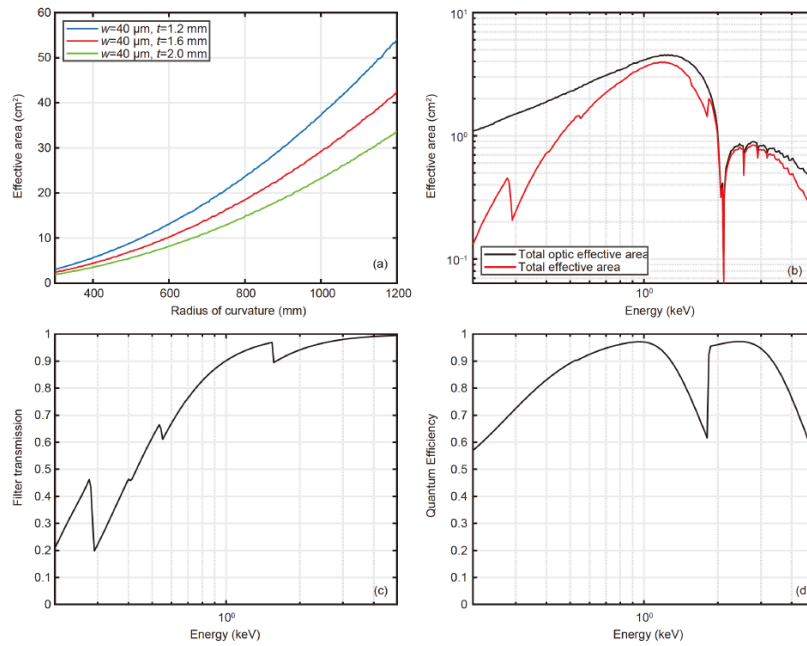


Figure 5 (a) Total effective area changes with radius of curvature, (b) The effective area changes with incident energy of X-ray, (c) SXI filter X-ray transmission curve, (d) SXI CCD QE curve

Table 2 LSXI main performance parameters

Parameter	Value
Energy range	200eV~2.5keV
Spatial resolution	~6arcmin (FWHM)
Optic coating	Iridium
Energy resolution	50eV@0.5keV

LSXI instrument includes four main parts: X-ray telescope, tracking turntable and two electronic boxes for telescope and turntable (Figure 6). The pointing stability provided by a tracking turntable.

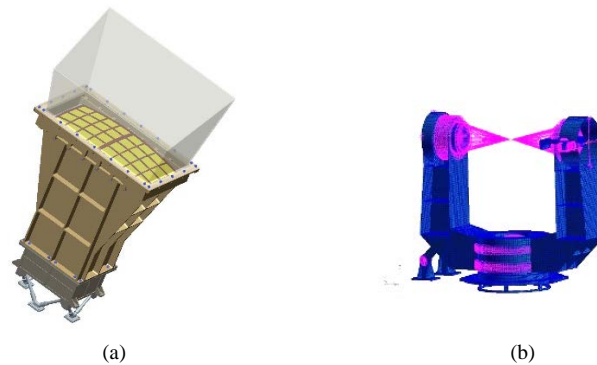


Figure 6 Concept configuration of (a) LSXI structure, (b) Tracking turntable structure

During the change of the relative position between the Moon and Earth, the turntable will track the observation area, and maintain the image stability. The electronic boxes for telescope and turntable are used for power management, working mode control, data storage and remote command execution of the instrument. Equipped with an earth sensor, the tracking turntable drives the X-ray telescope to achieve high-precision tracking and position maintenance.

4. Analysis and Simulation for LSXI

4.1 Orbit comparison

Comparing to the SMILE satellite's high elliptical polar orbit, LSXI will observe the magnetosphere from equatorial orbit, which results to a different observing range of the magnetosphere in the FOV. The FOV of SMILE is $16^{\circ} \times 27^{\circ}$, corresponding to the region $\sim 5.3R_E$ by $10.6R_E$ observed near the apogee with a geocentric distance of $20R_E$. LSXI will observe from $60R_E$ away with a similar FOV corresponding to the region $\sim 14.5R_E$ by $29R_E$, which will include the cusps and magnetopause in one picture. Meanwhile, the images captured on the Polar orbit observation mode, the north\south cusps will overlap, which is not beneficial to observing cusps regions. On the other hand, observing from an equatorial orbit can clearly separate the northern and southern cusps, and simultaneously include the northern and southern cusps into the FOV. In addition, two payloads, one on a polar orbit and one on an equatorial orbit can cooperate for simultaneous detection, and the joint observation could contribute enormously to the inversion of the three-dimensional configuration of the magnetopause.

4.2 Observing simulation

LSXI viewing angle at different positions in one lunar orbit (Figure 7). The orbit section marked in blue is the observing period, and the red part is the standby section as the sun stray-light will affect the detector and result in high temperature.

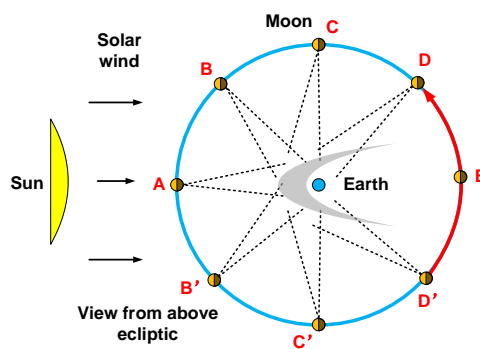


Figure 7 Observing geometry

In the previous work, we demonstrated the lobster-eye model and ray tracing method based on imaging simulation and magnetohydrodynamic (MHD) model [Peng et al., 2018; Sun et al., 2019; Sun et al., 2020]. Here, we use MHD model to simulate dayside magnetosheath X-ray intensity distribution [Wang et al., 2013]. The MHD images show the X-ray intensity distribution (Figure 8) corresponding to the position A, B, C (Figure 7). The lunar positions are A: (58.61, 1.33, -2.94) R_E , B: (44.06, -36.56, -6.39) R_E , C: (0.2, -57.69, 7.78) R_E . They are in the GSM coordinate system. The solar wind conditions are: solar wind number density $N=20\text{cm}^{-3}$; speed $V_X = 400\text{km/s}$; and interplanetary magnetic field (IMF) $B_X = 0$, $B_Y = 0$, $B_Z = -5\text{nT}$. The MHD simulation corresponds to 0.5 degree per pixel with FOV of $40^\circ \times 40^\circ$. Each MHD images consist of 81×81 point, every pixel is regarded as the point light source. The instrument results are simulated based on the MHD images (Figure 9). Please refer to previous work [Peng et al., 2018] for details of the simulation method. For the instrument image simulation, we use the lobster-eye optic parameters as following: the radius of curvature is 60 cm; micro-channel width and plate thickness are $40 \mu\text{m}$ and 1.2 mm; the reflectivity material is Ir with 0.5 nm surface roughness; the integration time of the three images is 300 second, and the average energy of one X-ray light is 0.5keV. The simulation results do not include the impact of background and instrument “noise”.

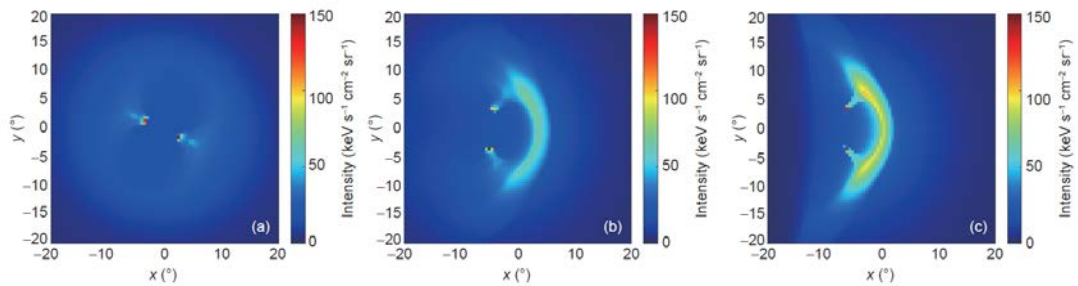


Figure 8 MHD simulation images describing the soft X-ray intensity distribution in a magnetic storm event, (a), (b), (c) are MHD simulation result corresponding to the respective positions A, B, C in Figure 7

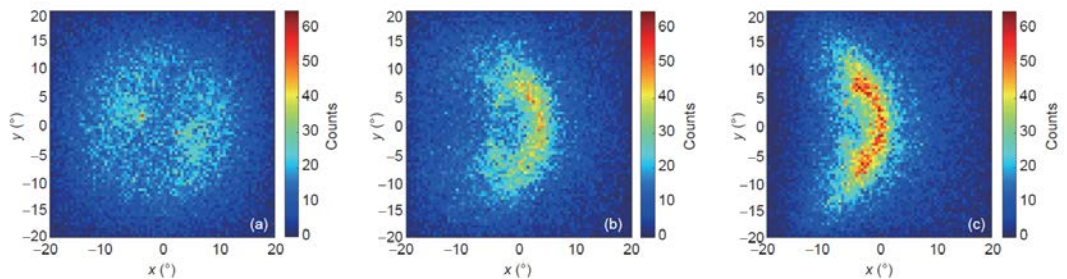


Figure 9 SXI instrument simulation images corresponding to Figure 8

Taking Figure 8 (c) as an example, the maximum emission intensity of magnetosheath

is around $100 \text{ keV/s/cm}^2/\text{sr}$. After imaging through the instrument, considering the influence of filter and CCD QE, the number of counts is around 40 in one pixel (0.5 degree) for an integration time of 300 seconds. Detector will be cooled to a low temperature to reduce the dark noise to a relatively low level in operation. However, SNR is more dependent on the solar wind state as it has a huge variation. Apart from this, the observation results are also affected by the sky background. In the soft X-ray band, the background is dominated by the diffuse astrophysical X-ray background. Particle induced background tends to dominate at higher X-ray energies. The contribution from discrete point sources is also much less than the diffuse component on large angular scales. An X-ray sky background tool, which calculates average X-ray background count rates from the ROSAT All-Sky Survey diffuse background maps, is available at NASA's High Energy Astrophysics Science Archive Research Center (HEASARC). The sky background will vary depending on the three view angles A, B, C (Figure 7), and its influence on observation results shall be reduced or possibly removed from the final imaging result of the magnetosphere. Using the aforementioned tools the intensity of the soft X-ray background is conservatively estimated to be around $50 \text{ keV/s/cm}^2/\text{sr}$ in the energy range of the LSXI. As the background at soft X-ray energies has a similar spectral shape to the SWCX emission the expected background counts is therefore around half that of SWCX emission in the maximum pixel, giving an approximate $\text{SNR} \sim 40 / \sqrt{40 + 20} \sim 5$ sigma for an integration time of 300 seconds in that pixel alone. The foreground SWCX emission is therefore easily detectable above background.

4.3 Settlement place analysis

Due to the particular geometry of the moon orbit, continuous and long-term observation can be achieved by setting up a Soft X-ray imager on the Moon. Based on the experience of space exploring projects, the site selection principles of lunar based observation are as follows. First, it shall ensure the safety and usability of the equipment. Second, based on a flexible location strategy, the scientific goal should be achievable [Mendell, 1985]. The influencing factors of lunar base site selection include topography, observation duration, communication capacity and energy demand etc. To observe the target from the lunar surface, two basic conditions shall be achieved: keeping the “nose” (i.e. the subsolar point on the magnetopause) in the FOV and avoiding Sun light incidence into the optics directly.

We choose three ideal locations on the Moon surface to estimate the observation time. They are the equatorial region (latitude: 0° , longitude: 0°), North Pole region (latitude: 80° , longitude: 0°), and South Pole region (latitude: -80° , longitude: 0°). We calculate

the observation time of the “nose”, “northern cusps” and “southern cusps” during 1095 days from Jan 1st 2021 to Jan 1st 2024 in three different locations. At the equatorial region, the independent observation time of nose and cusps is around 750 days, simultaneous observation time for nose and cusps is 727 days; at the Polar Regions, the simultaneous observation time decreases to 583 days. The continuous observation time in one month can be up to 20 days (Table 3). As a whole, either in the equatorial region or Polar Regions, adequate observation time can be obtained. These time consideration of the Sun constraints.

Table 3 observation time statistics in three different locations

Location (lat, long)	FOV	Observing time (Days)			
		Nose	N-Cusp	S-Cusp	Nose+Cusps
Equatorial region (0, 0)	15°×30°	752	738	740	727
N pole region (80, 0)	15°×30°	752	742	593	583
S pole region (-80, 0)	15°×30°	752	599	743	590

There are several potential advantages of establishing a lunar base in South Pole region. Compared with other regions of the Moon, there is a good thermal environment and the impact crater provides natural conditions for radiation protection [Jia and Zou, 2016]. Under Chinese Lunar Exploration Program Phase IV plan, scientists have proposed a vision to preliminarily build a research station on the lunar South Pole. According to the analysis (Table 3), there is sufficient continuous observation time for scientific goals. The Moon’s South Pole region can be used as a settlement location for LSXI. More detailed and comprehensive site selection analysis will be carried out in subsequent research.

5 Mission profile

For the preliminary design, LSXI will be placed on the Moon’s South Pole region. In order to obtain a global view of Earth’s magnetosphere we required a FOV of 15°×30° (Figure 10).

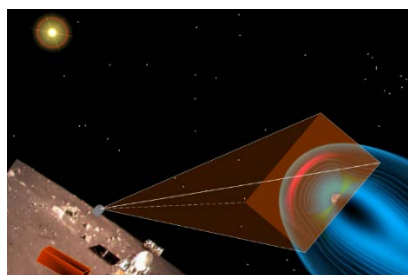
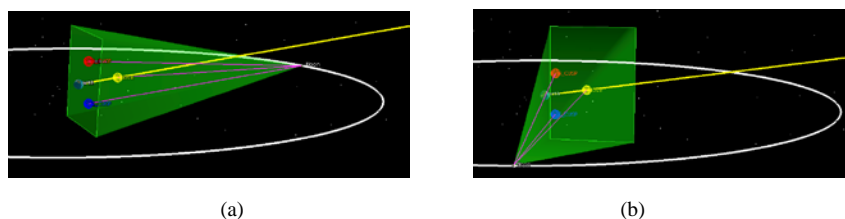
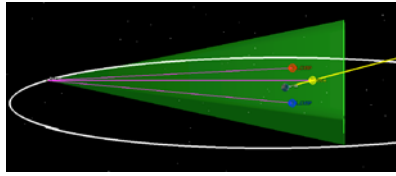


Figure 10 Concept artwork of observing the magnetosphere from the lunar surface

Compared with other orbital observation schemes, a lunar platform has many advantages. Firstly, the Moon is in synchronous rotation with Earth, and thus always shows the same side to Earth. Therefore, the Moon becomes an excellent location for achieving a near-continuous observation of the solar wind-magnetosphere region. Secondly, the Moon is about $60R_E$ away from the Earth. Therefore, the $15^\circ \times 30^\circ$ FOV of LSXI could cover the whole magnetopause region including the bow shock, magnetopause and cusps. It will enable the global monitoring of the dynamic process of solar wind-magnetosphere interaction. Thirdly, the Moon is a permanent and stable observation platform. Its life cycle is not as limited as that of satellites. It is able to cover one complete or more than the 11-year cycle of solar activity. The lunar surface is covered by dust, which will degrade the performance of the instrument. LSXI will be anticipated to have a door covering the aperture and once the dust has settled after being thrown up by the deployment system the door will be opened for normal operations. This door would also protect the instrument during transit. Furthermore, the electromagnetic shield will be anticipated to keep the lens surface clean and extend the lifetime of the instruments [Díaz, 2014]. The tracking turntable will be set to keep the telescope pointing at the magnetopause and cusps. At the same time, according to the observation requirements, an observation plan can also be set up by ground instructions to adapt to changes in different solar wind conditions.

The entire instrument package weighs about 35 kg (excluding the turntable and battery or the solar panel). The detector usually requires cooling to under $\sim 100^\circ\text{C}$ for optimum performance. An actively cooled system is needed. The estimated total power consumption is about 50 W. The power supply on the Moon is also an important issue. It takes about 29.5 days for the Moon to orbit the Earth, and the orbital plane nearly coincides with the ecliptic plane. In one orbital period (Figure 7), LSXI can achieve continuous observation in the blue segment phase for about 22 days, and stands by due to the direct sunlight in the red segment phase. Moon moves to different positions corresponding to the front, side and back views of the magnetosphere. Here, the red/blue balls represent the North/South Cusps, the yellow ball stands for the position of the subsolar magnetopause, and the yellow line is the Sun-Earth line (Figure 11).





(c)

Figure 11 3D simulation of changes in the moon's position

6 Summary

After successfully executing the early phases of CLEP, China is now proposing follow-up plans. In this paper, we have illustrated the concept of LSXI. Taking advantage of the position change between the Earth and Moon, LSXI will use the most advanced imaging technology to observe the global image of Earth's magnetosphere from multiple angles for a long time. Furthermore, combining space-based and ground-based detection results, it will bring profound innovations to the research of magnetospheric physics, and it has direct application in predicting and mitigating space weather disasters. This mission is aimed for launch around 2027. The LSXI mission is led by National Space Science Center, CAS, and in collaboration with institutions in China and abroad, including the Mullard Space Science Laboratory, University of Leicester (UK), and other research institutions.

Acknowledgments: We would like to give the gratefulness to the members of LSXI team. Thanks to colleagues who have always cared about the project and made valuable suggestions. The work is supported by the NNSFC grants 41731070, 41974211, 41774173, 41731070, Key Research Program of Frontier Sciences CAS, Grant No. QYZDJ-SSW-JSC028, Strategic Pioneer Program on Space Science, CAS, Grant No. XDA15052500, XDA15350201.

Reference

1. Angel J R P. 1979. Lobster eyes as X-ray telescopes. Space Optics Imaging X-Ray Optics Workshop. International Society for Optics and Photonics, 184: 84-85.
2. Bhardwaj A, Elsner R F, Gladstone G R, et al. 2007. X-rays from solar system objects. *Planetary and Space Science*, 55(9): 1135-1189.
3. Branduardi-Raymont G, Sembay S F, Eastwood J P, et al. 2012. AXIOM: advanced X-ray imaging of the magnetosphere. *Experimental Astronomy*, 33(2-3): 403-443.
4. Camps A. 2019. Nanosatellites and applications to commercial and scientific missions. *Satellites and Innovative Technology*. IntechOpen.
5. Collier M R, Porter F S, Siebeck D G, et al. 2012. Prototyping a global soft X-ray imaging instrument for heliophysics, planetary science, and astrophysics science. *Astronomische Nachrichten*, 333(4): 378-382.
6. Collier M R, Siebeck D G, Cravens T E, et al. 2010. Astrophysics noise: A space weather signal. *Eos, Transactions American*

- Geophysical Union, 91(24): 213-214.
7. Cravens T E. 1997. Comet Hyakutake X-ray source: Charge transfer of solar wind heavy ions. *Geophysical Research Letters*, 24(1): 105-108.
 8. Cravens T E. 2000. Heliospheric X-ray emission associated with charge transfer of the solar wind with interstellar neutrals. *The Astrophysical Journal Letters*, 532(2): L153.
 9. Credland J, Mecke G, Ellwood J. 1997. The Cluster mission: ESA's spacefleet to the magnetosphere. *Space Science Reviews*, 79(1-2): 33-64.
 10. Díaz Gilete S. 2014. Use of electrodynamic screens for performance optimization of optics and solar panels on the Moon's surface. Dissertation for Master Degree. Universitat Politècnica de Catalunya.
 11. Fujimoto R, Mitsuda K, McCammon D, et al. 2007. Evidence for solar-wind charge-exchange X-ray emission from the Earth's magnetosheath. *Publications of the Astronomical Society of Japan*, 59(sp1): S133-S140.
 12. Gotz D, Adami C, Basa S, et al. 2015. The microchannel x-ray telescope on board the SVOM satellite. arXiv preprint arXiv:1507.00204.
 13. Jia Y Z, Zou Y. 2016. Research on lunar site selection for lunar based earth observation. *Spacecr. Eng*, 25: 116-121.(in Chinese)
 14. Li C, Wang C, Wei Y, et al. 2019. China's present and future lunar exploration program. *Science*, 365(6450): 238-239.
 15. Lisse C M, Dennerl K, Englhauser J, et al. 1996. Discovery of X-ray and extreme ultraviolet emission from comet C/Hyakutake 1996 B2. *Science*, 274(5285): 205-209.
 16. Liu Z X, Escoubet P, Cao J B. 2005. A Chinese-European multiscale mission: the double star program. *Multiscale Coupling of Sun-Earth Processes*. Elsevier Science BV, 509-514.
 17. Mendell W W. 1985. Lunar bases and space activities of the 21st century. Lunar and Planetary Institute.
 18. Peng S, Wei F, Guo Y, et al. 2019. Preliminary geometric parameters optimization of lobster-eye-type wide field of view soft x-ray imager. *Optical Engineering*, 58(9): 093101.
 19. Peng S, Ye Y, Wei F, et al. 2018. Numerical model built for the simulation of the earth magnetopause by lobster-eye-type soft X-ray imager onboard SMILE satellite. *Optics express*, 26(12): 15138-15152.
 20. Robertson I P, Cravens T E. 2003. X-ray emission from the terrestrial magnetosheath. *Geophysical research letters*, 30(8).
 21. Schwadron N A, Cravens T E. 2000. Implications of solar wind composition for cometary X-rays. *The Astrophysical Journal*, 544(1): 558.
 22. Snowden S L, Collier M R, Kuntz K D. 2004. XMM-Newton observation of solar wind charge exchange emission. *The Astrophysical Journal*, 610(2): 1182.
 23. Sun T R, Wang C, Sembay S F, et al. 2019. Soft X-ray Imaging of the Magnetosheath and Cusps Under Different Solar Wind Conditions: MHD Simulations. *Journal of Geophysical Research: Space Physics*, 124(4): 2435-2450.
 24. Sun T R, Wang C, Wei F, et al. 2015. X-ray imaging of Kelvin-Helmholtz waves at the magnetopause. *Journal of Geophysical Research: Space Physics*, 120(1): 266-275.
 25. Sun T, Wang C, Connor H K, et al. 2020. Deriving the Magnetopause Position from the Soft X-Ray Image by Using the Tangent Fitting Approach. *Journal of Geophysical Research: Space Physics*, 125(9): e2020JA028169.
 26. Walsh B M, Collier M R, Kuntz K D, et al. 2016. Wide field-of-view soft X-ray imaging for solar wind-magnetosphere interactions. *Journal of Geophysical Research: Space Physics*, 121(4): 3353-3361.
 27. Wang C, Branduardi-Raymont G. 2018. Progress of solar wind magnetosphere ionosphere link explorer (SMILE) mission. *Chin. J.*

Space Sci., 38(5): 657-661.

28. Wang C, Guo X C, Peng Z, et al. 2013. Magnetohydrodynamics (MHD) numerical simulations on the interaction of the solar wind with the magnetosphere: A review. *Science China Earth Sciences*, 56(7): 1141-1157.
29. Wu W, Yu D, Wang C, et al. 2020. Technological breakthroughs and scientific progress of the Chang'e-4 mission. *Science China Information Sciences*, 63(10): 1-14.
30. Xu L, Zou Y L, Qin L. 2019. Overview of China's Lunar Exploration Program and Scientific Vision for Future Missions. *LPI*, (2132): 2440.
31. Yuan W, Zhang C, Ling Z, et al. 2018. Einstein Probe: a lobster-eye telescope for monitoring the x-ray sky. *Space Telescopes and Instrumentation 2018: Ultraviolet to Gamma Ray*. International Society for Optics and Photonics, 10699: 1069925.
32. Zhao W, Wang C. 2019. China's lunar and deep space exploration: touching the moon and exploring the universe. *National Science Review*, 6(6): 1274-1278.